Measurement and modelling of wall friction in the ram extrusion of stiff microcrystalline cellulose-based pastes

H.C. Ayton[1], S.L. Rough[1], M.P.F. Sutcliffe[2], P. Müller[3], J. Schäfer[3], D.I. Wilson[1]

[1] Department of Chemical Engineering and Biotechnology, University of Cambridge, Philippa Fawcett Drive, Cambridge, CB3 0AS, UK
[2] Department of Engineering, University of Cambridge, Trumpington Street, Cambridge, CB2 1PZ, UK
[3] Ceratizit Austria GmbH, Metallwerk-Plansee-Straße 71, AT-6600 Reutte, Austria

Abstract

Simulation of paste extrusion requires knowledge of the material–wall interactions and bulk deformation behaviour. A systematic approach to decoupling these is presented for a stiff paste, comprising microcrystalline cellulose/calcium carbonate/water, employing three different experimental configurations to separate paste-wall friction from bulk rheology. The bulk yielding behaviour was identified from ram extrusion testing with orifice dies, while wall friction was characterised using the twin-die extrusion apparatus reported by (Bryan *et al*., 2018). Further extrusion tests with square and conical entry dies featuring various die land lengths provided data for comparison with simulations. The wall friction exhibited non-linear Navier slip with negligible pressure dependency: this relationship was included within a solid mechanics-based simulation of ram extrusion with ABAQUS. The estimate of the plastic yield stress from orifice die testing was refined using simulations of flow through square-entry dies and predicted the extrusion pressure for conical-entry dies with reasonable accuracy.

Keywords : Extrusion, Modelling, Paste, Wall Slip

31 *Nomenclature*

Roman

A	Area	m^2
CED	Circular equivalent diameter	m
D	Diameter	m
D_0	Barrel diameter	m
D_1, D_2	Diameter of primary (1) and secondary (2) TSED die	m
E	Young's modulus	Pa
f	Number fraction	-
F	Cumulative number fraction	-
H	Height	m
H_b	Barrel height	m
H_e	Extrudate height	m
k_u	Herschel-Bulkley flow consistency	Pa $(s^{-1})^{-s}$
L	Length	m
L_0, L_1, L_2	Length of barrel (0), primary (1) and secondary (2) TSED die	m
m_1	Benbow-Bridgwater die entry flow index	-
n	Navier slip exponent, non-linear case	-
P	Pressure	Pa
$P_{\mathrm{T}1}, P_{\mathrm{T}2}, P_{\mathrm{T}3}$	Pressure ransducers 1, 2, 3	Pa
P_1	Benbow-Bridgwater die entry term	Pa
P_2	Benbow-Bridgwater die land term	Pa
P_central	Central transducer pressure (PT_2)	Pa
P_ex	Extrusion pressure	Pa
P_w	Pressure drop due to wall friction	Pa
R	Die radius	m
R_a	Arithmetic mean deviation of profile	m
R_f	Fillet radius	m
R_0	Barrel radius	m
s	Herschel-Bulkley flow index	-
t_test	Current test time	s
u_1, u_2	Displacement in x (1) and y (2) directions	m
V, $\lvert V \rvert$	Velocity, magnitude	m s^{-1}
V_1	Flow velocity in TSED initial die	m s^{-1}
V_ram	Ram velocity	m s^{-1}
V_chamber	TSED die chamber velocity	m s^{-1}
V_ex	Extrudate velocity	m s^{-1}
V_slip	Slip velocity	m s^{-1}
x	Displacement	m
y	Distance along sample path	m

32

Greek

α	Benbow Bridgwater die entry velocity multiplication factor	Pa (m s^{-1})$^{-m}{}_1$
β	Navier slip multiplication factor, non-linear	Pa (m s^{-1})$^{-n}$
β_s	Navier slip multiplication factor	Pa (m s^{-1})$^{-1}$
$\dot{\varepsilon}$	Strain rate	s^{-1}
η	Viscosity	Pa s
θ	Angle	radians
ϑ_{max}	Maximum cone die-entry angle	radians
μ	Coulombic friction coefficient	-
ν	Poisson's ratio	-
ρ	Density	kg m^{-3}
σ	Stress	Pa
σ_0	Herschel-Bulkley yield stress	Pa
σ_y	Yield stress	Pa
σ_{22}	Stress in vertical direction	Pa
τ	Shear stress	Pa
τ_w	Wall shear stress	Pa
$\tau_{w,b}, \tau_{w,d}$	Barrel and die land wall shear stress	Pa
τ_y	Shear yield stress	Pa
τ_0	Benbow-Bridgwater shear yield stress term	Pa

Abbreviations

ALE	Arbitrary Lagrangian-Eulerian
AR	Aspect ratio
BB	Benbow-Bridgwater method
$CaCO_3$	Calcium carbonate
CE	Conical-entry
CED	Circular equivalent diameter
CEL	Coupled Eulerian-Lagrangian
CFD	Computational fluid dynamics
CI	Confidence interval
FEA	Finite element analysis
LPM	Liquid phase migration
MCC	Microcrystalline cellulose
PEEK	Polyether ether ketone
PT	Pressure transducer
SE	Square-entry
SS	Stainless steel
TSED	Twin square entry die system

1. *Introduction*

Highly dense suspensions, with solids loading close to the particles' maximum packing fraction, are widely used in net shape forming operations to create shaped products with constant cross section. These are often known as 'pastes': the term 'dough' is used less often as it has a strong association with viscoelastic behaviour. Examples of such pastes include PTFE suspensions (Mitsoulis and Hatzikiriakos, 2009), microcrystalline cellulose/water wet masses used in pharmaceutical extrusion-spheronisation (Zhang *et al.*, 2011), and ceramic and hardmetal green body forming mixtures (Wilmot *et al.*, 2009), (Blackham *et al.*, 2012), (Ferstl *et al.*, 2012). The high solids fraction gives rise to yield stress behaviour and significant wall slip, both of which are features of plastic materials. The high yield stresses (orders of kPa) and often weak velocity dependence lead to them being described as 'stiff' and their behaviour is complicated by a number of effects related to their multi-phase nature (Wilson and Rough, 2012) which do not arise with viscoplastic fluids.

Ram extrusion has been employed both as an industrial process for forming paste materials and as a method to characterise their rheology. It involves pushing material through a contraction, or die, to generate an extrudate with a particular shape. In rheological testing it overcomes some of the problems arising with conventional rheometers but is accompanied by issues associated with loading (ensuring the sample is homogeneous and free of air pockets) and interpretation of the results. Figure 1 shows a schematic diagram of a simple laboratory ram extruder with key dimensions labelled, alongside a schematic showing the important contributions to the overall pressure drop (and force exerted on the ram, often used to calculate this quantity). The extrusion die depicted has a square-entry geometry,

meaning the die face is aligned at 90° to the barrel walls. A conical-entry die features an angle less than 90°.

Figure 1.

As with capillary rheometry, assumptions are required to extract rheological parameters from ram extrusion data. Benbow and Bridgwater (Benbow and Bridgwater, 1995) presented a semi-empirical model for the paste extrusion pressure, P_{ex}, assuming that (see Figure 1(b)) in the die entry (P_1) the paste deforms plastically with no redundant work, and only experiences significant wall shear in the die land (P_2), where it is assumed to undergo plug flow at velocity V_{ex} with complete slip at the walls, *viz*.

$$P_{\mathrm{ex}} = P_1 + P_2 = \underbrace{2(\sigma_0 + \alpha {V_{\mathrm{ex}}}^{m_1}) \ln\left(\frac{D_0}{D}\right)}_{\text{die entry}} + \underbrace{4\left(\frac{L}{D}\right)(\tau_0 + \beta {V_{\mathrm{ex}}}^{n})}_{\text{die land}} \quad (1)$$

The wall shear stress (τ_{w}) contribution to the pressure drop comprises a shear yield stress, τ_0, alongside a power-law velocity dependence described by empirical parameters β and n. Contributions from wall friction in the barrel are usually neglected. Deformation in the die entry was considered by Benbow and Bridgwater to involve simple extension, with the empirical parameters σ_0, α and m_1 describing the yielding behaviour. This approach works well for comparative purposes, but the parameters are not readily employed in detailed simulations of other geometries (Wilson and Rough, 2012).

Other analytical models for P_1 exist, including that of Basterfield *et al.* (Basterfield, Lawrence and Adams, 2005), who considered the flow of a viscoplastic Herschel-Bulkley material (obeying Equation (2)) with uniaxial flow consistency k_{u} and flow index s through a smooth-walled conical entry zone of angle $\vartheta_{\max}$ upstream of an orifice die (*i.e.* L = 0). The assumption of a smooth wall results in a regular radial velocity profile and allowed the local

extensional shear rate, $\dot{\varepsilon}$, to be calculated analytically, which could be integrated over the entry to give Equation (3).

$$\sigma = \sigma_0 + k_{\mathrm{u}}\dot{\varepsilon}^s \tag{2}$$

$$P_{\mathrm{ex,orifice}} = 2\sigma_0 \ln\left(\frac{D_0}{D}\right) + Ak_{\mathrm{u}}\left(\frac{2V}{D}\right)^s\left(1 - \left(\frac{D}{D_0}\right)^{3s}\right) \tag{3}$$

where

$$A = \frac{2}{3s}[\sin(\vartheta_{\max}).(1 + \cos(\vartheta_{\max}))]^s \tag{4}$$

Zhou *et al.* (Zhou *et al.*, 2013) used Basterfield *et al.*'s result to describe the extrusion behaviour of fresh cement paste. This model does not consider the work involved in the change in flow patterns upstream and downstream of the radial flow zone, or shear against the cone sides, which give rise to the more complex flow patterns suggested in Figure 2.

Figure 2.

Curved boundaries of the 'static zone' have been reported experimentally by visualisation techniques including sectioning of billets, magnetic resonance imaging (MRI) velocimetry (Barnes, Wilson and Johns, 2006), (Rabideau *et al.*, 2012), (Mantle *et al.*, 2004), nuclear magnetic resonance (NMR) imaging (Götz, Buggisch and Peciar, 1993), (Götz, Kreibich and Peciar, 2002), particle tracking, positron emission particle tracking, PEPT (Wildman *et al.*, 1999), and speckle velocimetry (Wilmot *et al.*, 2009).

(Bryan, Rough and Wilson, 2015) conducted detailed 2-D computational fluid dynamics (CFD) simulations of a viscoplastic (Herschel-Bulkley) fluid flowing through concentric cylindrical dies, quantifying the wall friction associated with wall slip using a Navier slip law, of the form

$$\tau_{\mathrm{w}} = \beta_{\mathrm{s}} V_{\mathrm{slip}} \tag{5}$$

They showed that the shape of the static zone in the die entry region, and hence the work involved in this deformation, was strongly affected by the wall friction. Flow visualisation and CFD simulation of solid granular soap extrusion was conducted by (Bryan, Rough and Wilson, 2017), who concluded that extraction of rheological parameters from ram extrusion testing was an ill-posed problem if only overall quantities (extrusion pressure, mean velocity and geometry) were available. Reliable identification of parameters either required local information (*e.g.* pressure measurements, velocity distributions from imaging) or additional experimentation.

Ram extrusion of pastes has also been modelled using solid mechanics approaches. Horrobin and Nedderman (Horrobin and Nedderman, 1998) used the ABAQUS finite element analysis (FEA) platform to simulate the extrusion of a plastic material obeying von Mises' law with yield stress σ_{y}, extruding through a smooth square-entry die while (Horrobin, 1999) investigated the influence of wall friction. They reported the following

$$\frac{P_1}{\sigma_{\mathrm{y}}} = 0.700\left(\left(\sqrt{26.8\ln\left(\frac{D_0}{D}\right)+1}\right)-1\right), \quad \left(1-\frac{D}{D_0}\right) < 0.6 \tag{6}$$

$$\frac{P_1}{\sigma_{\mathrm{y}}} = 1.92\ln\left(\frac{D_0}{D}\right)+1.08, \quad \left(1-\frac{D}{D_0}\right) > 0.6 \tag{7}$$

relationships for P_1 for smooth-walled dies:

Other solid mechanics studies include those of (Aydin *et al.*, 2000), who modelled conical-entry ram extrusion of an elasto-viscoplastic material with a combined Tresca and Coulombic friction law, while Patel *et al.* (Patel, Blackburn and Wilson, 2017) simulated the ram extrusion of a paste undergoing liquid phase migration (LPM). As with fluid mechanics approaches, constitutive relationships are required for bulk deformation (von Mises, Drucker-Prager, Cam-Clay for soils) and wall friction (*e.g.* Tresca, Coulombic). Model parameterisation is subject to the same challenge of the problem being ill-posed unless the wall is perfectly smooth or fully rough.

The parameterisation problem can be tackled by identifying wall friction relationships separately from overall extrusion behaviour. (Bryan, Rough and Wilson, 2018) investigated the frictional behaviour of a solid granular soap undergoing ram extrusion using novel devices to determine the wall slip behaviour. They then employed a fluid mechanics simulation technique to model the ram extrusion of the material, which led them to conclude that solid mechanics approaches could be more appropriate for granular materials like soap.

This paper implements the same approach, but with solid mechanics simulation. The extensional flow of the paste is modelled as a plastic material using ABAQUS. Experimental results are presented for a microcrystalline cellulose/calcium carbonate/water paste which is a model material for pharmaceutical extrusion (Zhang *et al.*, 2011). Experiments were conducted to identify the parameters associated with paste-wall friction and paste bulk rheological properties for extrusion in stainless steel equipment. The twin square-entry die (TSED) rig described by Bryan *et al*. (Bryan, Rough and Wilson, 2018) is used to identify wall friction behaviour as a function of bulk paste mean velocity in the chamber, assuming

incompressible plug flow and hydrostatic pressure, and the results are compared with values extracted from fitting ram extrusion data to Equation [1]. Contributions to P_{ex} from wall friction in the barrel and the die land are then subtracted to give an estimate of P_1. An ABAQUS simulation including the wall friction law is then used to refine the parameters to give a self-consistent set of properties for use in simulation of other geometries. As a test, parameters obtained from tests with square-ended dies are employed in simulations predicting the extrusion pressure for conical-entry dies.

Experimental Methods

1.1. Materials

The paste used in this study consisted of microcrystalline cellulose (MCC, Avicel PH101, FMC Corporation) and calcium carbonate ($CaCO_3$, Pumex V40-5) powders, with reverse osmosis water as the liquid binder. The MCC powder is often employed as a plastic forming aid (excipient) and the $CaCO_3$ was used as a means of making the paste stiffer (Zhang *et al.*, 2011).

The size and shape distributions of the MCC and $CaCO_3$ powders were characterised with a Morphologi G3 automated microscopy system. The circular equivalent diameters are presented in Table 1. Microscope images showed the MCC particles to be long while the $CaCO_3$ particles were more cuboidal. Further particle shape and size data are provided in the Supplementary Information.

Table 1

1.2. Paste Preparation

The paste composition is shown in Table 1. The method of preparation follows that of Zhang *et al.* (Zhang *et al.*, 2011). Mixing was performed with a Kenwood Chef planetary mixer equipped with a 'K'-shaped beater attachment.

The dry powders were first weighed out (± 0.01 g) and added to the mixer bowl. After one minute of dry mixing at mixer speed '0', water was slowly added to the bowl over a period of one minute. The mixing was continued at speeds '1', '2', '3' and '4' for 2, 3, 3 and 2 minutes, respectively. The bowl was scraped with a wooden spatula to remove paste from the walls between each mixing step. The paste was stored in a double-sealed container for at least 2 hours before use. A new batch of paste was prepared for each day of testing. The lab temperature and humidity were monitored and were found to vary between 19 and 24°C, 26 and 53%, respectively.

1.3. Extrusion Protocol

A Zwick ZO50 Strain frame configured as a ram extruder was used for paste extrusion experiments. The extrusion apparatus consisted of a stainless-steel barrel (25.00 mm inner diameter), ram (24.93 mm diameter, measured with digital callipers) with a polyether ether ketone (PEEK) tip, a brass extrusion table, and stainless-steel dies that sat in a recess in the table beneath the barrel. A number of stainless-steel dies were used for extrusion tests, all cylindrically concentric with diameter 3 mm. The die land lengths ranged from 0 (orifice dies) to 52 mm.

Prior to extrusion, a blank die was fitted, and the paste loaded into the barrel in 10 g charges, compacting each charge by hand before loading the next. Each test required approximately 90 g of paste. The ram was then lowered until it contacted the paste billet. The force was zeroed, and the billet compacted, lowering the ram at 0.2 mm s^{-1} until a

compaction force 500 N was recorded, and held at this level for 15 s. After compaction the ram was withdrawn, the blank die removed and the test die installed.

An extrusion run consisted of advancing the ram until it made contact with the paste. The force was zeroed and the ram moved downwards at the set speed. The force was measured by a load cell and the extrusion pressure calculated by dividing the measured force by the ram cross sectional area, *e.g.* $P_{\mathrm{ex}} = 4 \times (\mathrm{ram\ force})/\pi {D_0}^2$.

Six stainless-steel dies, with L/D = 52 mm / 3 mm, 40 mm / 3 mm, 28 mm / 3 mm, 10 mm / 3 mm, 3 mm / 3 mm and 0 mm / 3 mm were employed for the tests described in Section 4.1. Tests were conducted at five velocities, V_{ram} = 0.5, 1, 2, 3 and 5 mm s^{-1}, corresponding to V_{ex} = 34.7, 69.4, 139, 208 and 347 mm s^{-1}, respectively, (assuming the paste to be incompressible). Lower extrusion velocities were not used in order to avoid liquid phase migration. The orifice die tests described in Section 4.4 featured a wider range of velocities, from V_{ram} = 0.5 – 10 mm s^{-1} (V_{ex} = 34.7 - 694 mm s^{-1}).

Each extrusion profile showed an increase in the force measured by the ram as the paste moved into the die land until a steady state was reached, manifested as an approximately flat region on a plot of force vs ram displacement. The average extrusion pressure was taken over a region selected by eye such that any effects at the start and end of the test were excluded.

The system was converted to a conical geometry by inserting a stainless steel conical-entry section (height 11 mm, exit diameter 3 mm, cone angle 45 °) in the barrel above the die face. These tests were performed with dies with L/D = 42 mm / 3 mm and 12 mm / 3 mm.

206 1.4. Twin Stage Die Protocol

207 The twin square-entry die (TSED) rig (Bryan, Rough and Wilson, 2018), depicted in Figure 3,
208 consisted of two axisymmetric contraction regions separated by a cylindrical flow section.

209 Figure 3.

210 The extrusion setup was the same as for the normal extrusion tests, but with the TSED unit
211 replacing the square-entry die. The first chamber (D_1 = 11 mm, L_1 = 110 mm) had three
212 pressure transducer ports located along the chamber (Figure 3(a)). The secondary die, with
213 dimensions D_2 and L_2, was interchangeable and was secured in place by bolts.

214 The tests reported here employed three secondary dies, with L_2/D_2 = 35 mm / 3 mm, 22
215 mm / 3 mm, 10 mm / 3 mm. Five chamber velocities were tested, V_{chamber} = 10, 20, 30, 40
216 and 50 mm s^{-1} (corresponding to V_{ram} = 1.94, 3.87, 5.81, 7.74 and 9.68 mm s^{-1}, respectively).
217 Three lower velocities, V_{ram} = 0.1, 0.5 and 1 mm s^{-1} were also tested. In the 0.1 mm s^{-1} tests,
218 the extrusion pressure increased steadily over time and water leakage was observed
219 through the fittings, indicating that LPM was occurring (Mascia, Patel, Rough, Martin, &
220 Wilson, 2006).

221 Three Kulite XTM transducers (3.83 mm thread diameter, 35 MPa maximum operating
222 pressure, 45 MPa breakage pressure) were used to monitor the pressure along the TSED
223 chamber. They were calibrated with a Druck DPI digital pressure indicator using water as the
224 test medium. The voltages were sampled by LabView software using the DAQAssistant tool
225 at 2 Hz (V_{chamber} ≤ 30 mm s^{-1}), 3 Hz (V_{chamber} = 40 mm s^{-1}) and 4 Hz (V_{chamber} = 50 mm s^{-1}).
226 The averaging region was selected by eye by viewing each individual profile and choosing
227 the region that appeared to be in steady state. Since there were fluctuations in the

measured pressure due to the inhomogeneous nature of the paste, this selection was specific to each test.

The analysis of example TSED pressure transducer data is illustrated in Figure 4, for L_2/D_2 = 35 mm / 3 mm and V_{ram}= 3.87 mm s^{-1}. The pressure increased from zero to a maximum value in a period of approximately 5-6 seconds, corresponding to the filling of the TSED chamber with paste. The subsequent decrease from a maximum to a steady-state is hypothesised to result from the establishment of the flow profile and static zones within the device, which is commonly observed in paste extrusion profiles. There are often fluctuations and humps in the pressure measurements, attributed to paste inhomogeneity or the release of air bubbles trapped in the paste during loading and mixing. The steady-state region was selected as the portion of the profile after the initial transient response and before the decrease in pressure at the end of the test which displayed few large profile features and was as horizontal as possible. This was chosen manually (Figure 4(a)), as above, and the pressure readings averaged, giving a plot of pressure vs distance (Figure 4(b)). The 10^{th} and 90^{th} percentiles of the measured pressures in these regions were used as error bounds for the individual pressure measurements. A linear trend was fitted to the three pressure data points. The error in the linear fit was taken as the maximum and minimum gradient obtained through the error bounds.

Figure 4

1.5. Roughness Measurements

The roughness of the inner surface of the TSED bore was measured after polishing with a Talysurf i120 contact profilometer, using a stylus with a diamond tip of radius 2 μm. Three regions around the bore diameter were selected for testing. In each region, the roughness measurement was repeated over three 12 mm long axial traverses, centred on the pressure transducer ports. The cut-off length for roughness analysis was 2.5 mm and the traverse speed was 0.5 mm s^{-1}. The roughness heights of the polished inner TSED surfaces, characterised by the arithmetic mean deviations, R_a , are given in Table 2. All the values lie below R_a = 1 μm and are small compared to the characteristic powder sizes listed in Table 1. Fully rough behaviour, associated with particles being trapped within asperities on the die wall, was therefore not expected. Some light scoring was evident to the eye in the area behind each pressure transducer entry port, likely resulting from the machining of the part. All parts used in this study were either machined recently (dies, conical-entry insert), or polished prior to use (barrel, TSED).

Table 2

2. Theoretical and Computational Aspects

2.1. Wall shear stress estimation

The paste-wall shear stress can be estimated from the TSED measurements by a force balance, which gives

$$\tau_w = -\frac{D}{4}\frac{dP}{dx} \tag{8}$$

where x is the distance along the wall. It is assumed that the pressure is isotropic and uniform over the cross section. If the wall shear stress is independent of pressure and there

is complete slip in the die land (so that the paste is in plug flow, with V_{slip} being equal to the bulk paste plug flow velocity, V) a slip law of the form in Equation (1) can be postulated (Benbow and Bridgwater, 1995):

$$\tau_{\mathrm{w}} = \tau_0 + \beta V^n \tag{9}$$

This gives

$$\frac{\Delta P}{\Delta x} = -\frac{4}{D}(\tau_0 + \beta V^n) \tag{10}$$

where $\Delta P = P_2 - P_1$ and $\Delta x = x_2 - x_1$. Equation (9) could be adapted to include pressure dependency, with the inclusion of an extra term with μP, μ being an effective solid friction coefficient, as investigated by Bryan *et al*. (Bryan, Rough and Wilson, 2018), but minimal pressure dependence was observed for the MCC-based paste used here.

2.2. Computational Methods

2.2.1. Simulation Geometry

ABAQUS 6.14 (Dassault Systèmes, 2014), was used to simulate the flow of a plastic material in square- and conical-entry geometries and to estimate the pressure drop across the die entry region (Figure 2(c)).

Figure 5 shows the axisymmetric die-entry region. In all simulations, the barrel diameter was $2R_0$ = 25 mm, the die diameter $2R$ = 3 mm, the height of the billet H_{b} = 40 mm (to

incorporate static zones) and the extrudate height $H_{\mathrm{extrudate}}$ = 10 mm. The salient corner of the extrusion die was rounded slightly to avoid numerical issues associated with a square corner, with fillet radii of 0.3 mm and 0.6 mm for the square- and conical-entry simulations, respectively.

Figure 5

2.2.2. Analysis Method and Boundary Conditions

The simulation techniques adopted followed those used by (Dassault Systèmes, 2014) to model steady-state axisymmetric extrusion. An explicit solver with Arbitrary-Lagrangian-Eulerian (ALE) meshing and Eulerian boundaries was used. This avoided difficulty associated with mesh deformation that can occur with Lagrangian systems where large strains arise, whilst allowing the solid mechanics contact formulations to be used.

The boundary conditions were:

(i) The top boundary was rigid and a uniform vertical velocity was applied to this surface (see Fig. 5(a), (c));

(ii) An equation constraint was applied to the bottom boundary, such that the velocity normal to the boundary was uniform using the Abaqus *equation command (Dassault Systèmes, 2014), (see Fig. 5(c));

(iii) There was no displacement in the x direction along the centreline;

(iv) A power-law tangential friction condition of the form of equation 9 without normal stress dependence was set between the billet and barrel walls, finishing half-way around the filleted die corner. The second half of the fillet and the die land was prescribed as a frictionless contact condition, (see Fig. 5(c)).

Adaptive mesh constraints were:

(i) the top boundary was fixed in the x and y directions, and the bottom boundary in the *y* direction, to prevent mesh movement;

(ii) the inlet and outlet were set as Eulerian surfaces, enabling passage of material into and out of the mesh. The whole billet domain was set to be an ALE adaptive mesh domain.

Figure 5(a) and 5(c) outline the boundary conditions acting on the billet and the contact conditions. Figure 5(b) shows the adaptive mesh constraints which fixed and positioned the mesh.

2.2.3. Mesh Definition

Axisymmetric, linear, reduced integration, hybrid, constant pressure elements were used (Abaqus element type CAX4RH), employed in a structured quadrilateral mesh. The mesh was designed to be fairly uniform to prevent deformation as a result of the ALE remeshing. Around 13,000 elements were used for each square-entry extrusion simulation and 19,000 for conical-entry simulations. A global mesh seeding size of 0.2 mm was used: 30 mesh seeds were prescribed around the filleted die-entry corner for the square-entry simulation, and 8 for the conical-entry cases. The mesh was produced using the 'Medial-Axis' meshing technique for the square-entry simulations and the 'Advancing-Front' technique for conical-entry simulations. Examples of the meshes used for conical-entry and square-entry simulations are shown in Figure 6.

Figure 6

2.2.4. *Material and Frictional Properties*

The paste was modelled as a von Mises elastic-plastic material. The Poisson ratio was set at 0.47 to avoid high frequency noise in the simulation (Dassault Systèmes, 2014). The value of Young's modulus was found to have little impact on the important features of the solution, specifically the extrusion pressure and velocity profile. The Young's modulus was thus set at $150\times\sigma_{\mathrm{y}}$ to reduce simulation run-time and velocity fluctuation. Frictional heating was ignored.

The ABAQUS kinematic contact algorithm was used, with a friction law of the form of equation (8) encoded in the user subroutine VFRIC (see Supplementary Material) and parameters extracted from the TSED experiments.

The material density was scaled to decrease the simulation time, but not so much that the kinetic energy in the simulation became appreciable relative to the internal energy. A rule of thumb is that the kinetic energy should be less than 10% of the internal energy in each quasi steady-state simulation. Densities were chosen arbitrarily to ensure this was achieved, with 10^7 kg m^{-3} for V_{ram} < 1 mm s^{-1}, 10^6 kg m^{-3} for 1 ≤ V_{ram} ≤ 3 mm s^{-1}, and 10^5 kg m^{-3} for V_{ram} > 3 mm s^{-1}.

2.2.5. *Analysis Techniques and Results Extraction*

Python and MATLAB scripts were written to extract and plot the relevant data from ABAQUS. The energies at the sampling times were checked to avoid instances where significant mesh deformation was present. The MATLAB function '*griddata*' was used to interpolate the data to a regular grid with an element size in the *x* and *y* direction of $(\mathrm{size}/R_0) = 0.01$ and a linear interpolation scheme. The value of the grid element size was found to have little influence on the results and was selected to provide sufficiently accurate

detail of the features of the simulation (using an element size a little smaller than the mesh size in simulation, 0.125 mm).

The extrusion pressure was calculated by integrating the normal stress acting in the axial direction, σ_{22}, across a horizontal plane in the barrel located at $1.5R_0$ upstream of the die

$$P_{\mathrm{ex}} = \frac{1}{\pi R^2} \int_0^{R_0} 2\pi r \sigma_{22} dr \tag{11}$$

entry for square-entry and $1.5R_0 + H_{\mathrm{c}}$ for conical-entry simulations, *viz*.

The frictional shear stress was calculated from the stress outputs from billet elements in contact with the barrel and die walls.

2.2.6. Simulation Checks

Simulations were run with an Intel® Core™ i7-8700 CPU @ 3.20 GHz, 3192 MHz, 6 Core, 12 logical processors for a simulated extrusion time of 45 s. The actual time taken to compute the simulations depended on the simulation density, varying between approximately 1 day and 1 week. Convergence to a steady state was assessed by considering the plastic strain (PEEQ) at a node on the billet mesh adjacent to the die at the top (immediately after the filleted radius) and end of the extrudate section of flowing material (see Figure 5(a)). The kinetic, internal, plastic dissipation and other energies were also checked. The kinetic energy was found to be less than 300 times the internal energy in each simulation, indicating that there was little effect of the scaled density on the solutions. The effect of mesh size was tested with billet seed sizes of 0.1 –0.5 mm for a square entry case (V_{ram} = 3 3 mm s^{-1}) and found to give little difference in P_{ex}: a value of 0.2 mm was selected as a compromise between run-time and simulation quality. Alongside these factors, the linear and bulk

viscosity parameters in the ABAQUS simulation were set to zero and the averaging regions were selected to avoid times at which mesh deformation became significant.

3. Results and Discussion

The experimental results obtained with regular extrusion dies are presented in Section 4.1, which includes a Benbow-Bridgwater characterisation. Barrel friction tests are discussed in Section 4.2 and compared with wall friction results from the TSED device in Section 4.3. Section 4.4 presents experimental data obtained with orifice dies, which are compared with simulation results in Section 4.5.

3.1. Benbow-Bridgwater Approach

Six stainless-steel square-entry extrusion dies were used to characterise the extrusion behaviour of the MCC/$CaCO_3$ paste. The results of extrusion tests with these dies at five test velocities are shown in Figure 7. The linear dependency on L/D indicates that τ_w was constant along the selected die land (see Equation (1)) at a given velocity, and independent of pressure. The intercepts on the y-axis give the Benbow-Bridgwater P_1 terms and these are summarised in Figure 8 (a). P_1 is approximately independent of velocity, indicating that the material could be described as plastic. The gradients from Figure 7 yield the wall shear stress, τ_w, and Figure 8 (b) shows a power-law dependency on V_{ex} of the form of equation (8).

Figure 7

Figure 8

3.2. Barrel friction tests

396 The contribution to the measured extrusion pressure from wall friction in the barrel was
397 determined by preparing a billet of paste as in the extrusion tests discussed above, then
398 using the ram to push it out of the barrel with no die in place. The force on the ram
399 (expressed as extrusion pressure) decreased linearly with displacement and the barrel wall
400 shear stress was estimated from

$$\frac{dP_{\mathrm{ex}}}{dx} = -\frac{2}{R_0}\tau_{\mathrm{w}} \tag{12}$$

401 The maximum velocity which could be tested in the strain frame was 10 mm s^{-1}. The τ_{w}
402 results obtained from these tests are shown in Figure 9 and lie around the power-law fit
403 discussed in Figure 11. The general trend is that τ_{w} increases with slip velocity.

404 Figure 9

405

406 *3.3. Twin Die Extrusion*

407 The TSED results in Figure 10 again show an increase in τ_{w} with estimated slip velocity,
408 following a power-law trend. The middle transducer pressures (PT_2 reading) ranged from 2.5
409 - 19.1 MPa in these tests and there was little effect on τ_{w} when L_2/D_2 was changed. This
410 was consistent with the linearity of the Bagley-like plots in Figure 7, indicating negligible
411 pressure dependence and little Coulombic contribution to the wall friction for this paste.

412 Figure 10

413 The three sets of wall shear stress data (Figure 8(b), Figure 9, Figure 10) were combined and
414 fitted to the empirical friction law (Equation 8). Figure 11 shows significant overlap between
415 the three data sets. The parameters from the fitting are reported in Table 3. Also shown on
416 the plot and in Table 3 are the results for related pastes (an MCC/water formulation, a

kaolin clay and a terracotta paste) obtained using the Benbow-Bridgwater approach. They all exhibit power-law behaviour, with 0.33 < *n* < 0.6. The material studied by (Zhang *et al.*, 2011) has some similarity to the paste studied here, lacking $CaCO_3$, and the range of V_{ex} tested was limited to $40 \leq V_{\mathrm{ex}} \leq 3100$ mm s^{-1}, as tests at lower speeds were subject to LPM. They were not able to justify a non-zero wall shear yield stress, τ_0: one of the advantages of the TSED device is the ability to access behaviour at low extrusion speeds reliably. Power-law slip relationships have also been reported for highly dense suspensions by He *et al*. (He, Lee and Kalyon, 2019) who used polydispersed mixtures of ballotini to prepare suspensions in a silicone oil (poly(dimethyl) siloxane) with solids volume fractions in the range 0.62-0.82.

Figure 11

Table 4

3.4. Orifice Die Extrusion

Orifice die tests provide insight into the work associated with die entry (and the yield stress) and provided data for comparison with the simulation results. Extrudates exhibited visually detectable fracture, as illustrated in the insert in Figure 12, with the fracture behaviour being determined by the ram velocity. The summary of extrusion pressures in Figure 12 shows a modest increase in P_{ex} with V_{ram}. Also shown is the expected τ_{w} contribution to P_{ex} for a 100 mm billet length (which would occur approximately half-way through each extrusion test), which mirrors the observed increase with V_{ram}. This is consistent with the paste behaving plastically, with paste-barrel wall friction exhibiting velocity dependence. There is some scatter in the data, most likely due to the inhomogeneous nature of the paste, which is exacerbated by the lack of a die land and a modest extrusion pressure.

Figure 12.

3.5. Simulations

3.5.1. Estimating the yield stress

Direct measurement of the yield stress is not possible, so σ_y was estimated by comparing P_{ex} values obtained from orifice die experiments (Section 4.4) with simulations. An initial estimate of σ_y was made using a truncated form of equation 1, $P_{ex} = 2\sigma_0 \ln\left(\frac{D_0}{D}\right)$ (assuming little velocity dependence). The estimate was compared with the steady-state simulation result (Equation 13) with an additional contribution for barrel wall friction in the region above the die entry as this was not considered in the simulation, *viz*.

$$P_{ex,sim} = P_{1,sim} + P_{barrel\ friction} = P_{1,sim} + 4\frac{H_{b,corrected}}{D_0}(\tau_0 + \beta V^n) \quad (13)$$

H_b was set at 81.25 mm which, when added to the length of the barrel with active friction in the simulation, gave a total billet height of 100 mm, which corresponded to a point midway through the extrusion test. Setting σ_y = 0.38 MPa gave reasonable agreement, shown in Figure 12. This value is less than that given by the Benbow-Bridgwater method (fitting data to Equation (1), which gave $\sigma_0 = 0.6$ MPa in this case, and $\sigma_0 = 0.5$ MPa for similar pastes (Parkin *et al.*, 2016)). One of the reasons why Equation (1) overestimates σ_y is because the expression used to estimate the extensional work, $2\sigma_0 \ln\left(\frac{D_0}{D}\right)$, does not consider redundant work. Employing Equation (6) instead, which was obtained from simulation of extrusion through smooth, square-ended dies, gave an estimate of 0.41 MPa. This is noticeably closer to the value obtained using the simulations and is slightly larger, which is expected as the contribution from wall friction to the experimental value acts in addition to the work required to yield the paste.

460

461 3.5.2. Flow patterns and shear stress results

462 Figure 13 presents streamline data for square-entry and conical-entry simulations. This
463 information is useful for identifying regions of high strain and strain rates, which can affect
464 the local microstructure and subsequently extrudate quality. Plug flow occurs in the barrel
465 and die land sections, shown here by the parallel streamlines in the barrel section. The
466 streamlines extend close to the die-barrel corner of the square-entry die, Figure 13(a),
467 which matches experimental observations in which the paste static zone did not extend
468 across the whole die face. Figures 13 (b) and (d) show contours of the von Mises stress.
469 These show that the section closest to the die land, extending to the barrel-die corner, is
470 under yield (giving values of the Von Mises stress equal to the yield stress, σ_y) but the
471 boundary of this region is rather flat, unlike the profile assumed in analytical treatments
472 such as Figure 2(b). Some fluctuations in the contour plots were observed with simulated
473 time, in particular along the walls of the barrel. One of these is labelled with an asterisk in
474 Figure 13(b). These are attributed to mesh movements or velocity/frictional fluctuations,
475 related to the ALE meshing present in the simulation. The von Mises plots for the square-
476 and conical-entry simulations are qualitatively similar. The same contour scale is used for
477 each.

478 Figure 13

479 The results can be compared with square- and conical-entry flow visualisation of solid soap
480 extrusion, reported by (Bryan, Rough and Wilson, 2017), in which a hemicylindrical flow
481 chamber was used to investigate the flow pattern in square-entry and conical-entry (30°
482 cone angle) geometries. A simulation was run for this cone angle using the MCC/$CaCO_3$

483 paste material parameters, and the results are compared in Figure 14. Good qualitative
484 agreement was obtained for both geometries, with material flowing close to the die-barrel
485 corner in each case.

486 Figure 14

487 Sets of velocity profiles for the square-entry simulations are presented in Figure 15(a),
488 sampled along the centreline of the billet. The frictional shear stress (ABAQUS *CSHEAR1*
489 parameter) is sampled along the elements of the billet in contact with the walls of the barrel
490 and die. This is plotted against distance along the barrel/die walls from the top right-hand
491 side of the billet, shown in 15(b). The maximum and minimum velocities in the simulations
492 closely match the estimates of the outlet velocities, assuming incompressible homogeneous
493 plug flow in the barrel inlet and outlet, shown by dotted lines in Figure 15(a). There are
494 small fluctuations in the values along the barrel and die- land region.

495 Figure 15

496 The computed τ_w values match the estimates fairly well in the barrel until $y/R_0 > 2$. As the
497 barrel-die corner is approached, the shear stress decreases, corresponding to the low-
498 velocity corner zone. The shear stress increases again as the die entry is approached and the
499 local velocity increases.

500

501 3.5.3. Conical entry dies

502 Simulations of the die-entry and experiments were conducted for dies with D = 3 mm, with
503 L = 16 mm and L = 42 mm, for different ram velocities. Neither of these die lands were used
504 in characterisation testing. P_{ex} included contributions from cone and barrel friction

505 ($P_{\mathrm{w,barrel}}$), the die entry, P_1, and die land friction, P_2. The latter was the largest of the three
506 contributions, corresponding to approximately 71% of the pressure drop for V_{ram} = 1 mm s^{-1}
507 and L/D = 42 mm / 3 mm.

508 Figure 16 compares the experimental data with the simulation results for this geometry.
509 Also shown are the P_{ex} values estimated using the Benbow-Bridgwater result for a conical-
510 entry die (excluding barrel friction) (Benbow and Bridgwater, 1995), *viz*.

$$P_{\mathrm{ex}} = 2(\sigma_0 + \alpha V^m + \tau_0 \cot\vartheta_{\mathrm{max}}) \ln\left(\frac{D_0}{D}\right) + \frac{\beta V^n}{n}\left(1 - \left(\frac{D}{D_0}\right)^{2n}\right)\cot\vartheta_{\mathrm{max}} + P_2 \qquad (14)$$

511

512 where ϑ_{max} is the angle of the cone wall to the axis of symmetry.

513 Figure 16

514 The simulation and Benbow-Bridgwater prediction give reasonable agreement with the
515 experimental data for the shorter die. The difference between the Benbow-Bridgwater
516 prediction and the simulation, arising from the P_1 term, was small. Both overestimate P_{ex}
517 for the longer die at higher velocities. This difference is attributed to differences in the
518 surface-roughness in the die lands from those used in the characterisation and TSED tests.
519 Since the die land pressure drop in these cases is the largest contribution to P_{ex}, and the
520 contribution increases with V_{ex}, this difference is manifested at higher speeds. The extrusion
521 pressure recorded at V_{ex}= 342 mm s^{-1} for a square entry configuration is plotted in Figure 7
522 and lies noticeably below the fitted trend line, indicating that this die differs from the
523 characterisation set.

Figure 16 indicates that Equation (14) gives a reasonable prediction of the extrusion pressure but the Benbow-Bridgwater approach gives no information about local flow behaviour and is not readily applied to complex geometries. Equation (3), by comparison, assumes a radial convergent flow pattern and thus could be employed to give rheological parameters for use in simulations. The radial flow is compared to the simulation results in Figure 17. The local velocity magnitude was calculated across two planes upstream of the die entry and this is plotted in normalised form, scaled by V_{ram}. The scaled radial flow field is independent of V_{ram}: the simulation results obtained for different velocities were similar so only one set is presented for clarity.

Figure 17

The flow field is expected to approach the radial case near the die entry. Figure 17 (a,ii) shows that this is the case for the square-entry die at h/R_0= 0.14, with the analytical profile slightly underpredicting the simulation result at the centreline. Wall friction has a small effect on the simulation profiles at this location, indicating that the wall was relatively smooth. Horrobin (Horrobin, 1999) showed significant differences when the wall was fully rough. In contrast, the two profiles differ markedly at h/R_0= 0.44 (Figure 17 (a,i)), with both simulation results indicating that the paste is still close to plug flow. This suggests that Equation (3) will not give a reliable estimate of the paste rheological parameters in this geometry even when there is significant slip at the walls.

In the conical entry case, a near-radial flow field is imposed by the geometry. Figure 17(a,ii) shows that the analytical profile gives a reasonable description of the flow pattern at h/R_0= 0.44, distant from the die entry. At lower h/R_0, the local velocity and wall shear stress increase, invalidating the assumption of frictionless lubricated flow in the analytical profile.

Figure 17(b,ii) shows that this causes significant differences between the analytical and simulated velocity profiles at h/R_0 = 0.16. It is noteworthy that the smooth-walled simulation differs from the analytical profile.

4. *Conclusions*

The wall friction behaviour of a MCC/$CaCO_3$ paste undergoing extrusion was quantified using ram extrusion and the friction rig developed by Bryan *et al*. (Bryan, Rough and Wilson, 2018). There was negligible effect of pressure on the wall shear stress and the data obtained from three different testing protocols showed good consistency. The data could be fitted to a non-linear Navier slip law including a shear yield stress, as proposed by (Benbow and Bridgwater, 1995). These tests featured a wide range of slip velocities and were able to access low velocities without encountering liquid phase migration problems.

Orifice die experiments were used to estimate the paste yield stress using solid mechanics simulations on ABAQUS employing an ALE meshing technique, custom VFRIC friction law and elastic-plastic material model. The bulk rheology of the paste could be described by a single value of the yield stress, indicating simple plastic behaviour. The yield stress of the paste was determined as 0.38 MPa and this was tested in simulations of ram extrusion through conical entry dies. The match with experimental data was good, indicating that the approach could be used to predict the flow through more complex dies. Comparison of the detailed flow profiles highlighted the challenges with using analytical results to estimate paste yielding behaviour from ram extrusion tests.

Acknowledgements

Project funding from Ceratizit GmbH is gratefully acknowledged.

Bibliography

Aydin, I. *et al.* (2000) 'Physical and numerical modelling of ram extrusion of paste materials: conical die entry case', *Computational Materials Science*. Elsevier, 18(2), pp. 141–155. doi: 10.1016/S0927-0256(00)00098-7.

Barnes, E. C., Wilson, D. I. and Johns, M. L. (2006) 'Velocity profiling inside a ram extruder using magnetic resonance (MR) techniques', *Chemical Engineering Science*. Pergamon, 61(5), pp. 1357–1367. doi: 10.1016/j.ces.2005.08.032.

Basterfield, R. A., Lawrence, C. J. and Adams, M. J. (2005) 'On the interpretation of orifice extrusion data for viscoplastic materials', *Chemical Engineering Science*, 60(10), pp. 2599–2607. doi: 10.1016/j.ces.2004.12.019.

Benbow, J. J. and Bridgwater, J. (1995) 'Paste flow and extrusion, {Oxford} series on advanced manufacturing, 1993', *AIChE Journal*, 41(3), p. 741. doi: 10.1002/aic.690410333.

Blackham, B. *et al.* (2012) 'The Effect Of Solids Loading On The Performance Of Extrusion Feedstock Of Cemented Carbide', in *The European Powder Metallurgy Association*. https://media.proquest.com/media/pq/classic/doc/3129883521/fmt/pi/rep/NONE?cit%3Aauth=Blackham%2C+Ben%3BBlackburn%2C+Stuart%3BRowson%2C+Neil%3BAl-Dawery%2C+Ihsan&cit%3Atitle=Hardmetals+-+Processing%3A+The+Effect+Of+Solids+Loading+On+The+...&cit%3Apub=Euro.

Bryan, M. P., Rough, S. L. and Wilson, D. I. (2015) 'Investigation of static zones and wall slip through sequential ram extrusion of contrasting micro-crystalline cellulose-based pastes', *Journal of Non-Newtonian Fluid Mechanics*, 220, pp. 57–68. doi: 10.1016/j.jnnfm.2014.08.007.

Bryan, M. P., Rough, S. L. and Wilson, D. I. (2017) 'Flow visualisation and modelling of solid soap extrusion', *Chemical Engineering Science*. doi: 10.1016/j.ces.2017.07.028.

Bryan, M P, Rough, S. L. and Wilson, D. I. (2017) 'Flow visualisation and modelling of solid soap extrusion', *Chemical Engineering Science*, 173, pp. 110–120. doi: https://doi.org/10.1016/j.ces.2017.07.028.

Bryan, M. P., Rough, S. L. and Wilson, D. I. (2018) 'Measurement of the wall slip behaviour of a solid granular soap in ram extrusion', *Powder Technology*. Elsevier, 323, pp. 76–85. doi: 10.1016/j.powtec.2017.09.053.

Dassault Systèmes (2014) 'Axisymmetric extrusion: transient and steady-state', in *ABAQUS V. 6.14 Examples Problems manual*.

Ferstl, H. *et al.* (2012) 'Influence of visco-elastic binder properties on ram extrusion of a hardmetal paste', *Journal of Materials Science*, 47(19), pp. 6835–6848. doi: 10.1007/s10853-012-6627-4.

Götz, J., Buggisch, H. and Peciar, M. (1993) 'NMR imaging of pastes in a ram extruder', *Journal of Non-Newtonian Fluid Mechanics*. Elsevier, 49(2–3), pp. 251–275. doi: 10.1016/0377-0257(93)85004-T.

Götz, J., Kreibich, W. and Peciar, M. (2002) 'Extrusion of pastes with a piston extruder for the determination of the local solid and fluid concentration, the local porosity and saturation and displacement profiles by means of NMR imaging', *Rheologica Acta*, 41(1–2),

615 pp. 134–143. doi: 10.1007/s003970200012.

616 He, J., Lee, S. S. and Kalyon, D. M. (2019) 'Shear viscosity and wall slip behavior of dense
617 suspensions of polydisperse particles', *Journal of Rheology*, 63(1), pp. 19–32. doi:
618 10.1122/1.5053702.

619 Horrobin, D. J. (1999) *Theoretical aspects of paste extrusion*. University of Cambridge. doi:
620 10.17863/CAM.31191.

621 Horrobin, D. J. and Nedderman, R. M. (1998) 'Die entry pressure drops in paste extrusion',
622 *Chemical Engineering Science*. Pergamon, 53(18), pp. 3215–3225. doi: 10.1016/S0009-
623 2509(98)00105-5.

624 Mantle, M. D. *et al.* (2004) 'Laminations in ceramic forming - Mechanisms revealed by MRI',
625 *Acta Materialia*. Pergamon, 52(4), pp. 899–909. doi: 10.1016/j.actamat.2003.10.026.

626 Mitsoulis, E. and Hatzikiriakos, S. G. (2009) 'Steady flow simulations of compressible PTFE
627 paste extrusion under severe wall slip', *Journal of Non-Newtonian Fluid Mechanics*. Elsevier,
628 157(1–2), pp. 26–33. doi: 10.1016/j.jnnfm.2008.09.003.

629 Parkin, J. *et al.* (2016) 'Experimental validation of a dimensional analysis of spheronisation of
630 cylindrical extrudates', *Powder Technology*. Elsevier B.V., 298, pp. 73–83. doi:
631 10.1016/j.powtec.2016.05.007.

632 Patel, M. J., Blackburn, S. and Wilson, D. I. (2017) 'Modelling of paste ram extrusion subject
633 to liquid phase migration and wall friction', *International Journal for Numerical Methods in
634 Engineering*, 172, pp. 487–502. doi: 10.1002/nme.2040.

635 Rabideau, B. D. *et al.* (2012) 'Internal flow characteristics of a plastic kaolin suspension
636 during extrusion', *Journal of the American Ceramic Society*, 95(2), pp. 494–501. doi:
637 10.1111/j.1551-2916.2011.04882.x.

638 Wildman, R. D. *et al.* (1999) 'Investigation of paste flow using positron emission particle
639 tracking', *Powder Technology*. Elsevier, 103(3), pp. 220–229. doi: 10.1016/S0032-
640 5910(99)00019-4.

641 Wilmot, R. B. *et al.* (2009) 'Characterisation and Design of Wax-Based Hard Metal Extrusion
642 Processes', *Plansee Seminar*. Reutte, Austria. Available at:
643 http://scholar.google.com/scholar?hl=en&btnG=Search&q=intitle:Characterisation+and+de
644 sign+of+wax-based+hard+metal+extrusion+processes#0.

645 Wilson, D. I. and Rough, S. L. (2012) 'Paste engineering: Multi-Phase materials and multi-
646 phase flows', *Canadian Journal of Chemical Engineering*. Wiley Subscription Services, Inc., A
647 Wiley Company, 90(2), pp. 277–289. doi: 10.1002/cjce.20656.

648 Zhang, M. *et al.* (2011) 'A comparison of ram extrusion by single-holed and multi-holed dies
649 for extrusion-spheronisation of microcrystalline-based pastes', *International Journal of
650 Pharmaceutics*. Elsevier, 416(1), pp. 210–222. doi: 10.1016/j.ijpharm.2011.06.043.

651 Zhou, X. *et al.* (2013) 'Rheology of semi-solid fresh cement pastes and mortars in orifice
652 extrusion', *Cement and Concrete Composites*, 37(1), pp. 304–311. doi:
653 10.1016/j.cemconcomp.2013.01.004.
654

Figure(s)

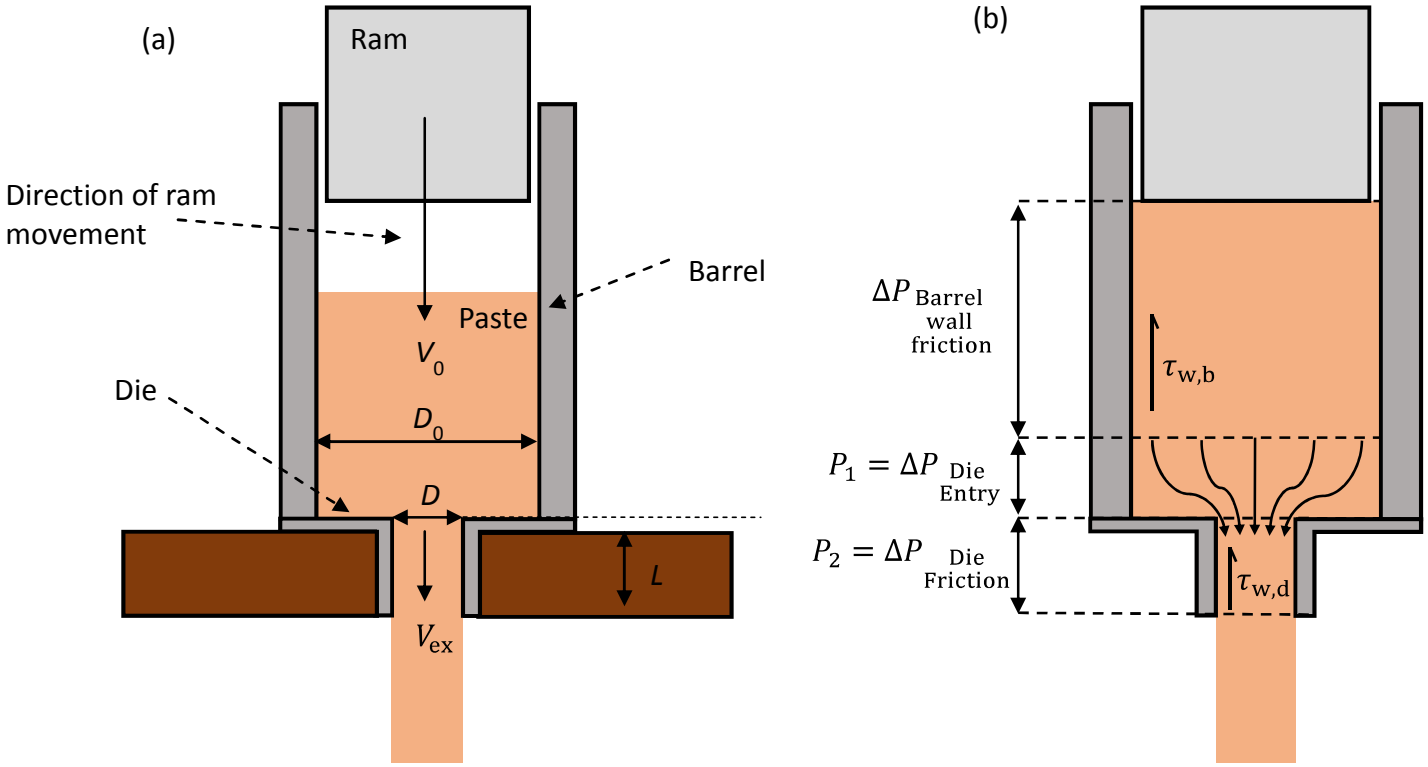

Figure 1. (a) Schematic of a ram extruder, showing the ram - used to push the paste through the shaped hole within a square entry die (SED), the barrel (housing initially containing the paste) and the die, alongside important dimensions and parameters. **(b)** Schematic showing contributions to the pressure drop, namely friction against the barrel and die walls and deformation in the die entry.

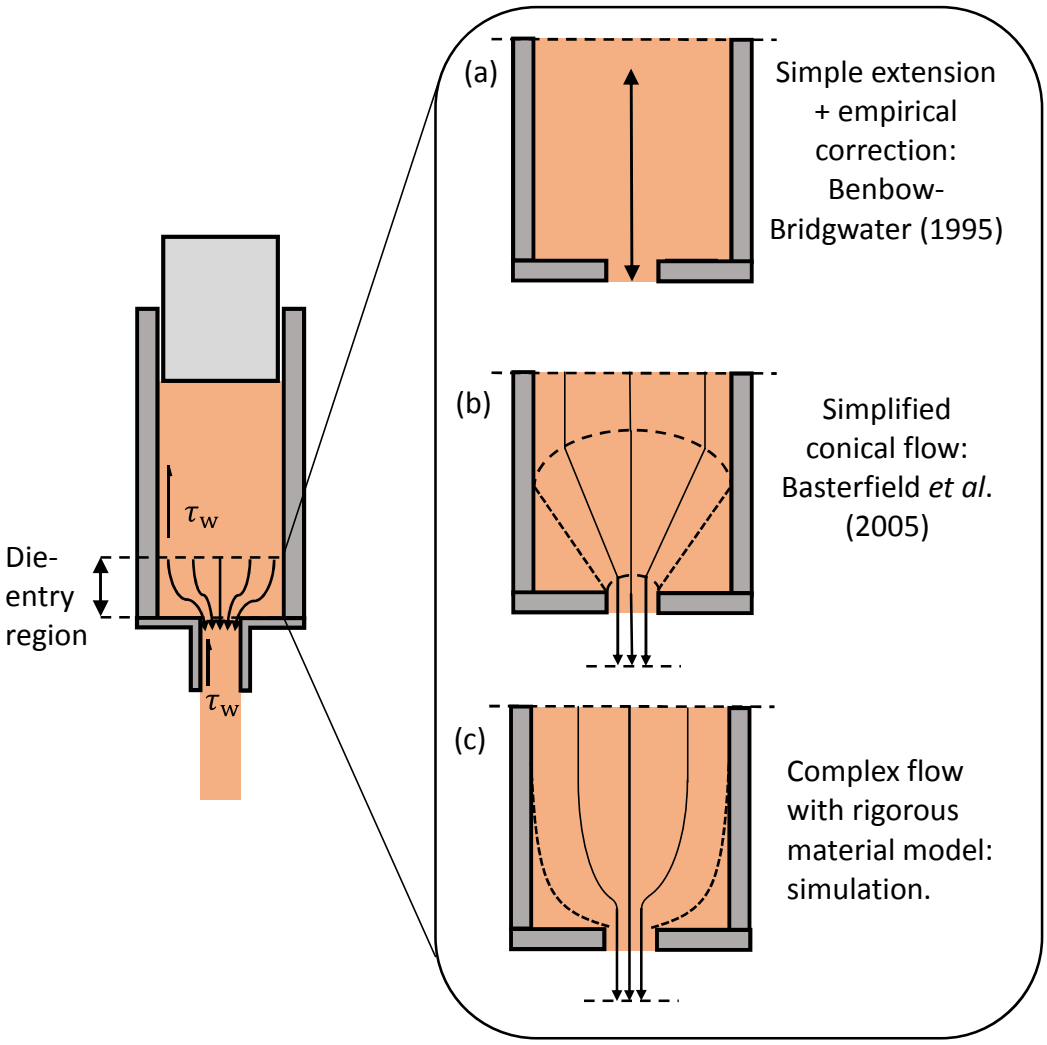

Figure 2. Schematics of paste flow through a square entry die showing different descriptions of extension. (a) Benbow-Bridgwater, flow field not defined; (b) conical convergent flow, *e.g*. (Basterfield, et al., 2005); and (c) flow profiles predicted by numerical simulation.

Table 1. Composition of the MCC/$CaCO_3$ paste.

Component	Mass fraction %	Number averaged circular equivalent diameter (CED) / µm
MCC	40.45	9.1
$CaCO_3$	49.44	7.3
water	10.11	-

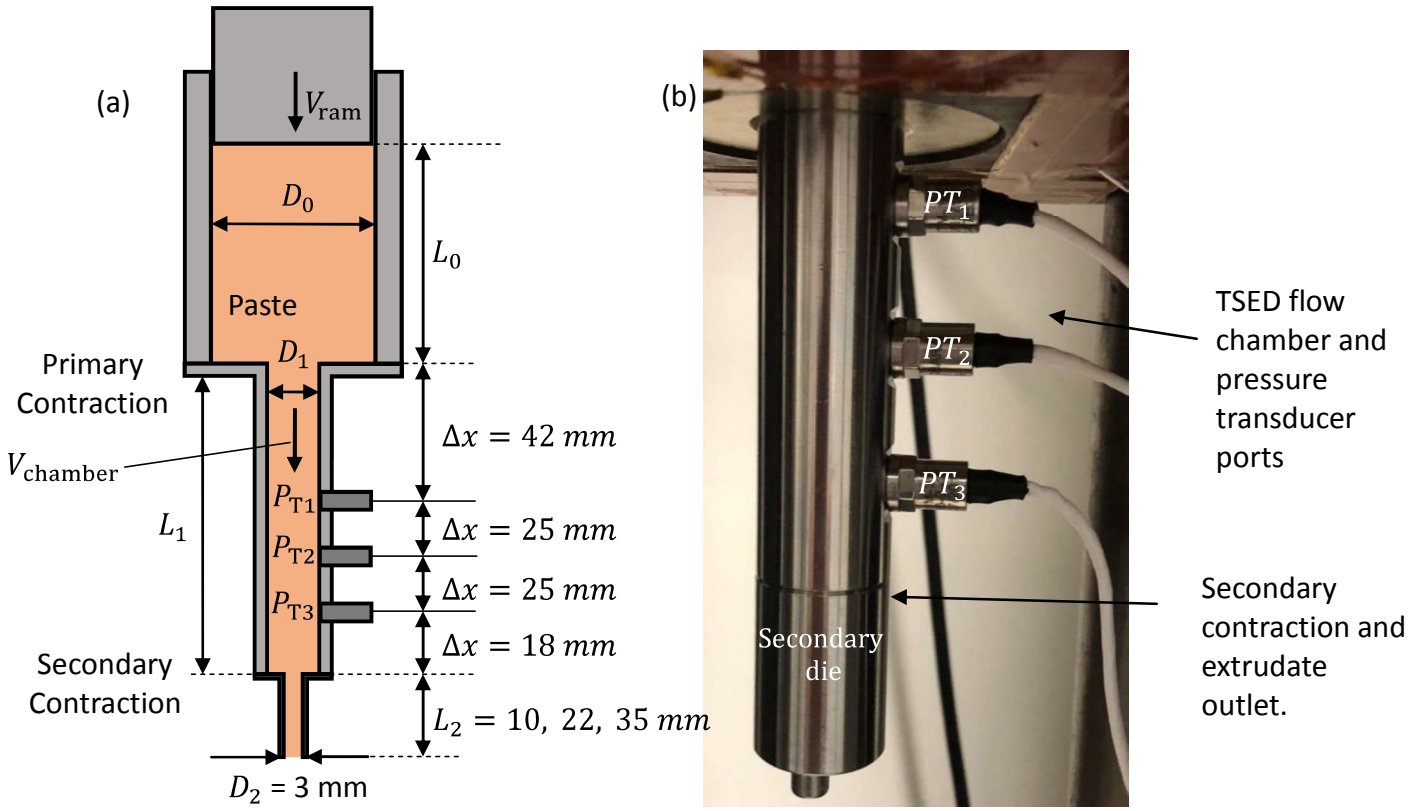

Figure 3. (a) Schematic diagram of the inner chambers of the TSED showing the internal dimensions and flow parameters. **(b)** Photograph of the TSED showing transducer ports and secondary die.

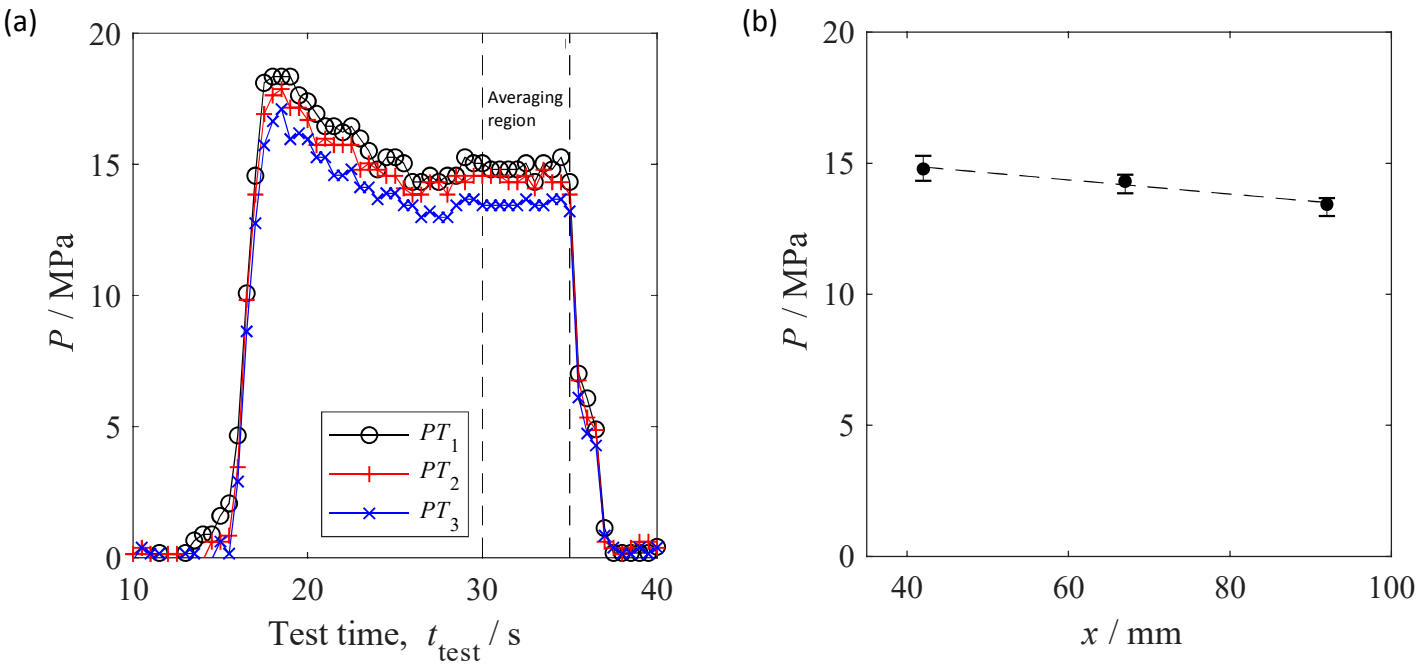

Figure 4. Example of data sets from TSED transducers for a test with L/D = 35/3 and V_{ram}= 3.87 mm s^{-1}: (a) pressure record; (b) average pressure vs distance along the TSED flow chamber, at locations shown in Figure 3(a). The error bars in (b) indicate the 90th and 10th percentiles for the pressure readings within the extrusion averaging region. The dotted line indicates the linear fit.

Table 2. R_{a} values measured at different locations on the TSED chamber wall.

Test Location		R_{a} / μm	$R_{\mathrm{a}}(\mathrm{mean})$ / μm
Hole 0	Centre	0.29	0.70
	90 ° Clockwise	0.81	
	90 ° Anticlockwise	0.99	
Hole 1	Centre	0.40	0.36
	90 ° Clockwise	0.32	
	90 ° Anticlockwise	0.35	
Hole 2	Centre	0.27	0.30
	90 ° Clockwise	0.34	
	90 ° Anticlockwise	0.29	

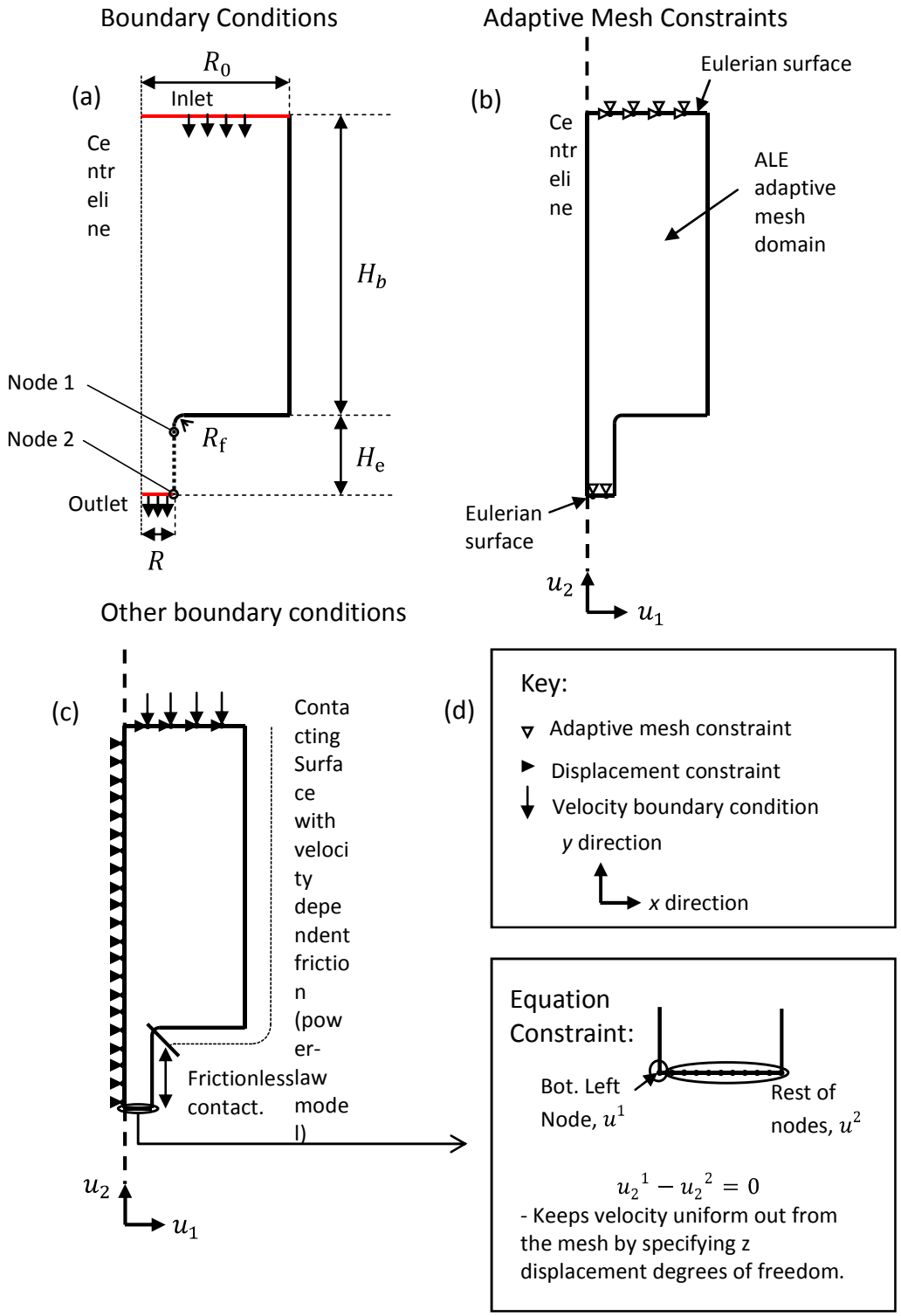

Figure 5. Die-entry simulation created using ABAQUS. **(a)** schematic diagram outlining the velocity inlet and outlet boundary conditions and the position of the centreline / axis in the square-entry simulations; **(b)** adaptive mesh constraints used in the model to fix and position the mesh during the analysis. **(c)** displacement / equation boundary conditions and contact specifications and **(d)** key describing the meaning of the symbols used and the equation constraint. Nodes 1 and 2 represent elements used to test the steady state by viewing the PEEQ at nodes on their outside edge (see section 3.2.6.).

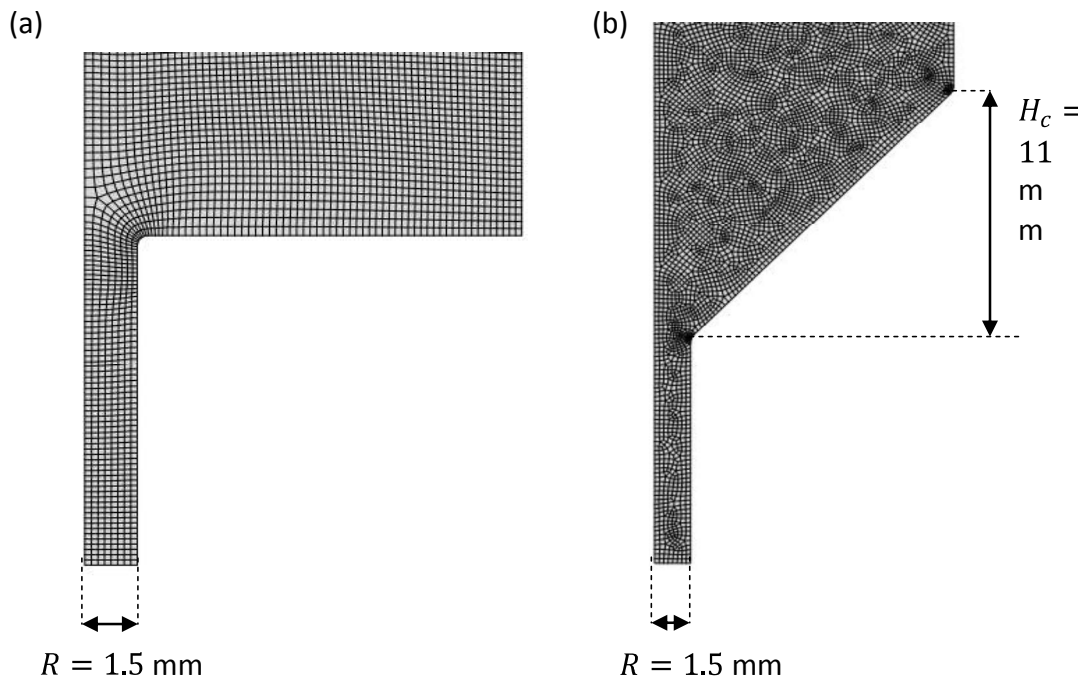

Figure 6. Meshes used for die-entry square- (a) and conical-entry (b) extrusion simulations. These meshes correspond to the deformed billet once any initial mesh movement had ceased.

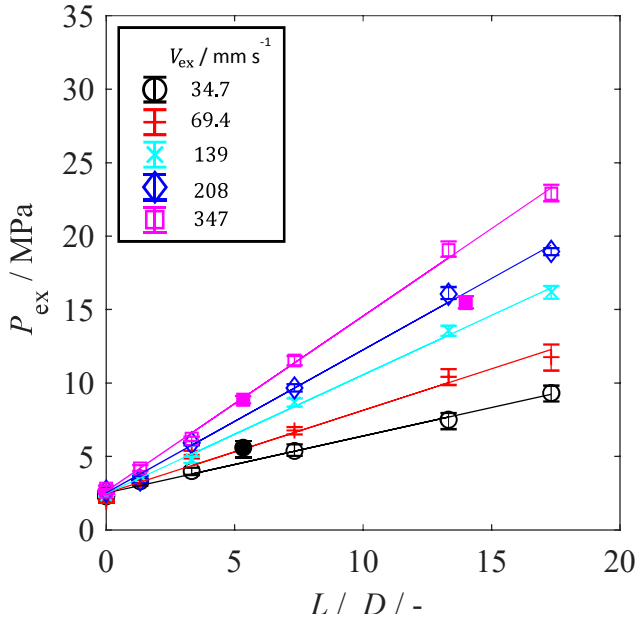

Figure 7. Bagley-style plots for extrusion of the MCC/$CaCO_3$ paste at the extrudate velocities indicated in the legend. Error bars represent the 10th and 90th percentiles of P_{ex} within the steady-state region of each data set. The loci show linear fits to the data. The solid points (purple squares, L/D = 5.33; black circle L/D = 14) relate to tests with dies not used in the characterisation, discussed in section 4.5.3.

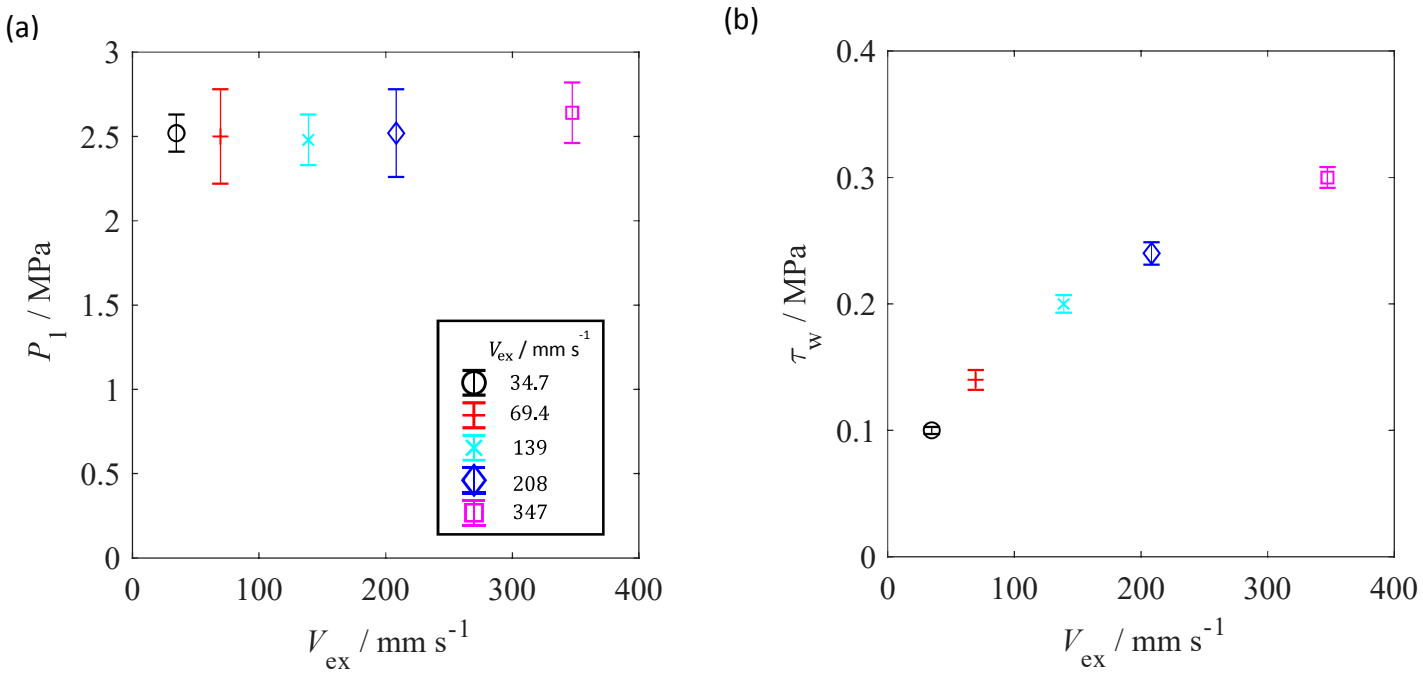

Figure 8. Benbow-Bridgwater analysis of data in Figure 7: (a) intercept, giving P_1 and (b) gradient, giving τ_w, as a function of V_{ex}. The error bars are those associated with the linear fits made to the data in Fig. 7.

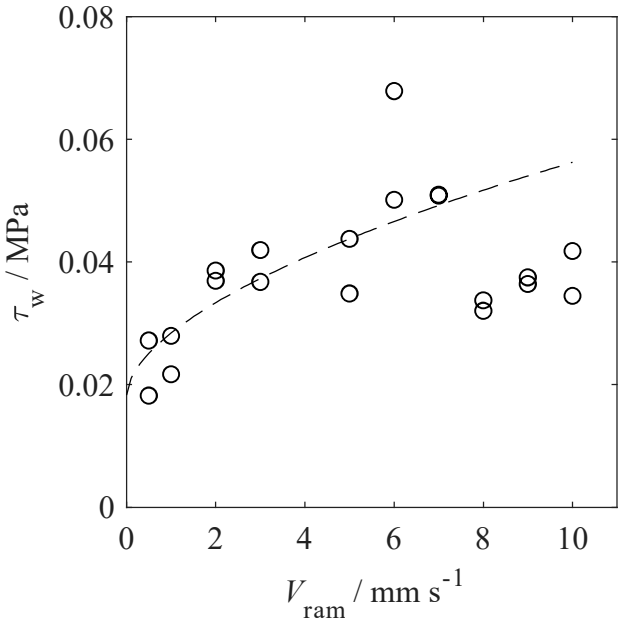

Figure 9. Effect of ram (billet) velocity on barrel wall shear stress. Error bars were smaller than the data points and are calculated based on the linear fit to the pressure profiles obtained. The dashed locus shows the friction law obtained for the tests in sections 4.1-4.3, shown in Figure 11.

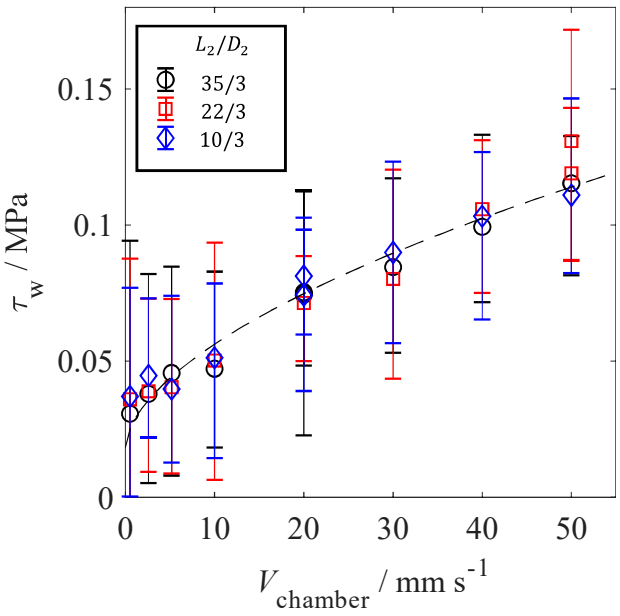

Figure 10. Wall slip measurements from TSED device, including repeated tests. Legend indicates secondary die dimensions. Range bars are calculated based on the maximum and minimum gradient through the range bars of the average pressures during the steady state regions (10^{th} and 90^{th} percentiles used). The dashed locus shows the friction law obtained for all tests in sections 4.1-4.3, shown in Figure 11.

Table 3. Parameters for wall slip law (equation 8) obtained by fitting to the TSED, Benbow-Bridgwater and barrel friction experimental data. Also shown are the wall slip relationships reported for related materials.

Material \ Parameter	τ_0 / Pa	β / Pa (m s^{-1})$^{-n}$	*n* / -	R-squared / -
This work, MCC/$CaCO_3$/water paste	1.8×10^4	5.4×10^5	0.58	0.979
95 % Confidence Interval (CI) lower	1.2×10^4	4.9×10^5	0.52	-
95 % CI upper	2.5×10^4	5.8×10^5	0.63	-
Zhang *et al*. (2011) 45 wt% MCC/water paste	-	3.4×10^5	0.33	-
Wildman *et al*. (1999) white kaolin clay paste	-	9.5×10^5	0.44	-
Guilherme *et al*. (2009) terracotta paste	5.0×10^3	4.8×10^5	0.58	-

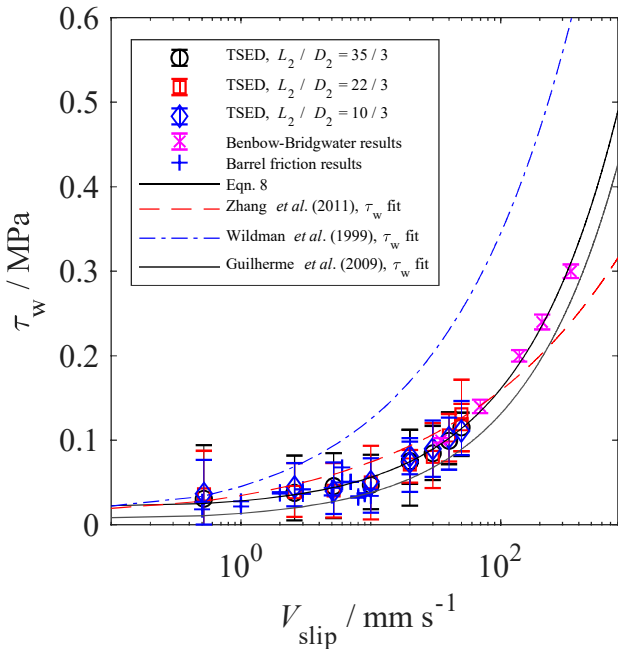

Figure 11. Combined wall slip data sets. Symbols: billet – circles; TSED – triangles; squares – ram extrusion (Figure 8(b)). Note log scale for V_{slip}. The solid black line shows fit to Equation (8) with parameters in Table 3. The error bars are those described previously. Dashed loci show the friction relationships reported for related materials listed in Table 3.

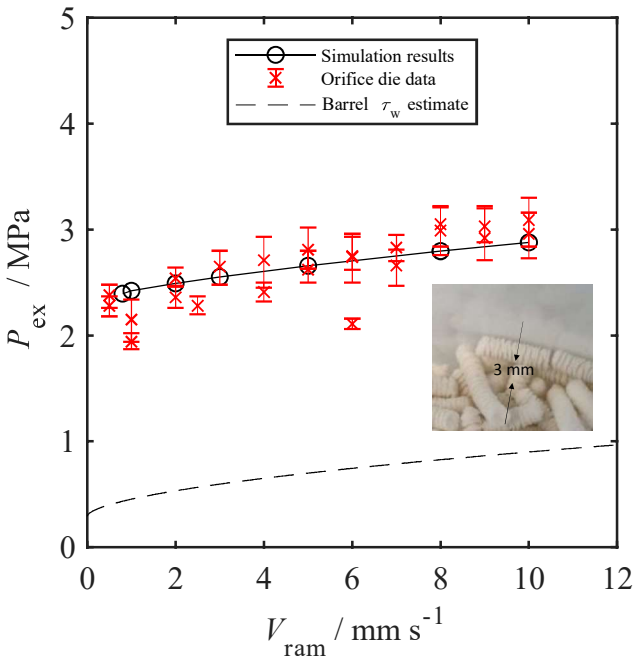

Figure 12. Effect of ram velocity on extrusion pressure for square-entry orifice dies with D = 3 mm. Simulation results - open black circles and solid black line; experimental data - red crosses. The simulation results include a barrel friction correction, calculated using Equation (8) for a 100 mm high paste billet. The error bars represent the 10th and 90th percentiles of the extrusion pressure in the region averaged for the data (as in previous Figures). Black dashed locus shows the estimated contribution to P_{ex} from barrel wall friction. Insert image shows an example of fractured extrudate.

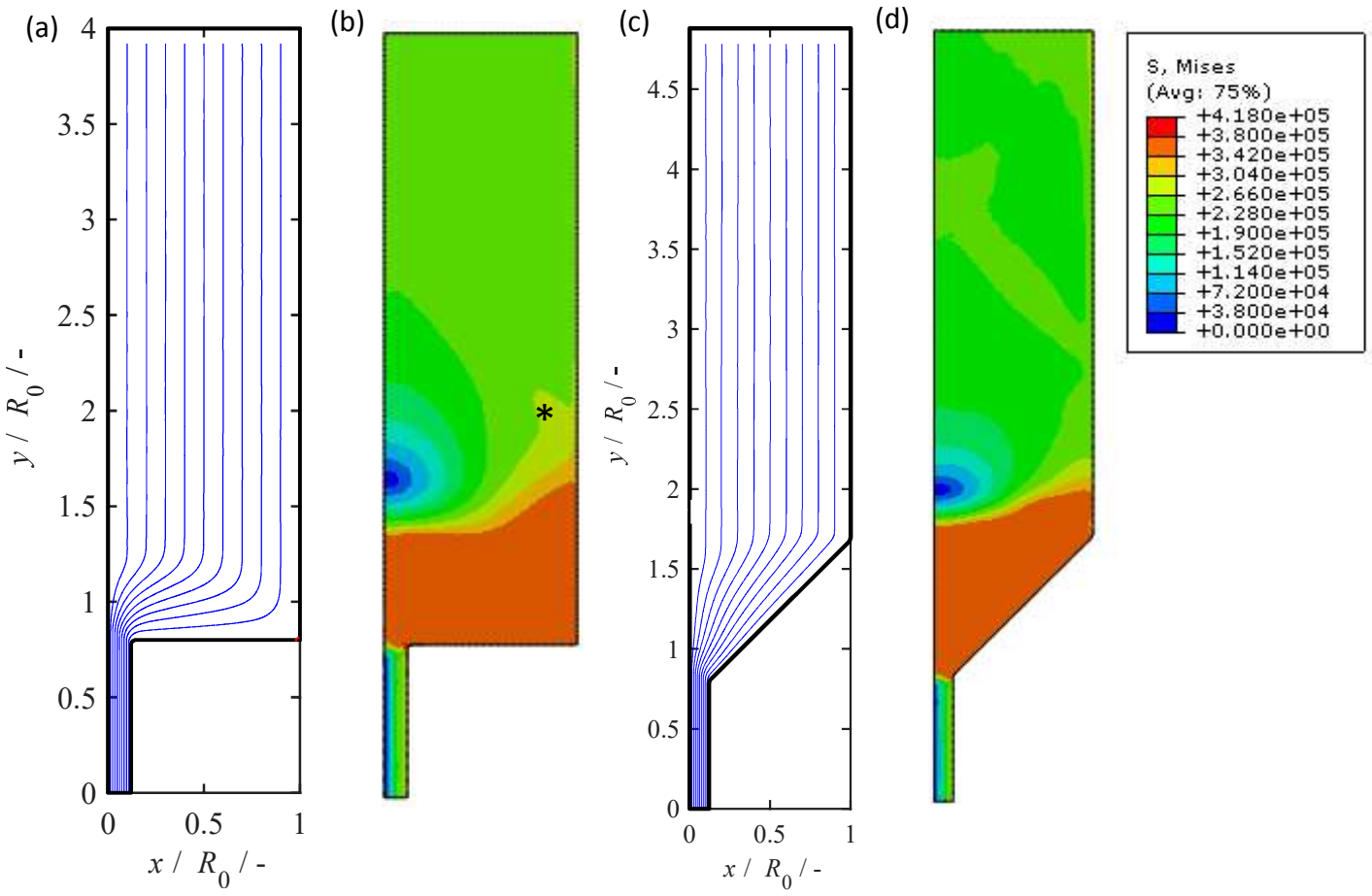

Figure 13. Examples of detailed simulation outputs. Streamlines for (a) square entry and (c) conical entry die, angle = $45°$, with power-law friction law (Equation (8)). (b) and (d) show the corresponding contour plots for the von Mises stress, sampled at the 120th frame in the simulation (simulation time of 27 s). Conditions: V_{ram} = 1 mm s^{-1}, D = 3 mm and $D_0 = 25$ mm. In the streamline plots, the solid black line shows the boundary of the die and barrel. Distances are scaled with $R_0 = D_0/2$. In the contour plots, some fluctuations in the contours with time were observed, expected to result from mesh movement or fluctuations in friction / velocity. One such fluctuation is labelled by an asterisk in (a).

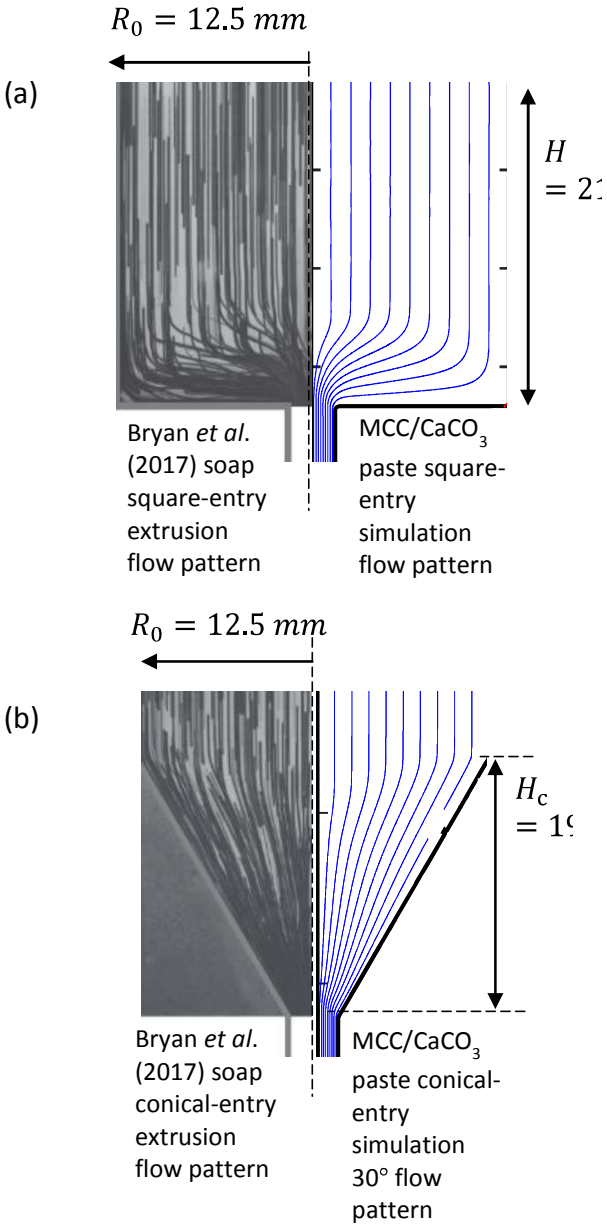

Figure 14. Comparison of simulation flow patterns to flow visualisation data from (Bryan, Rough and Wilson, 2017), for solid granular soap in (*a*) square-ended and (*b*) $30°$ conical-entry die geometries. In both cases, D = 3 mm and $D_0 = 25$ mm.

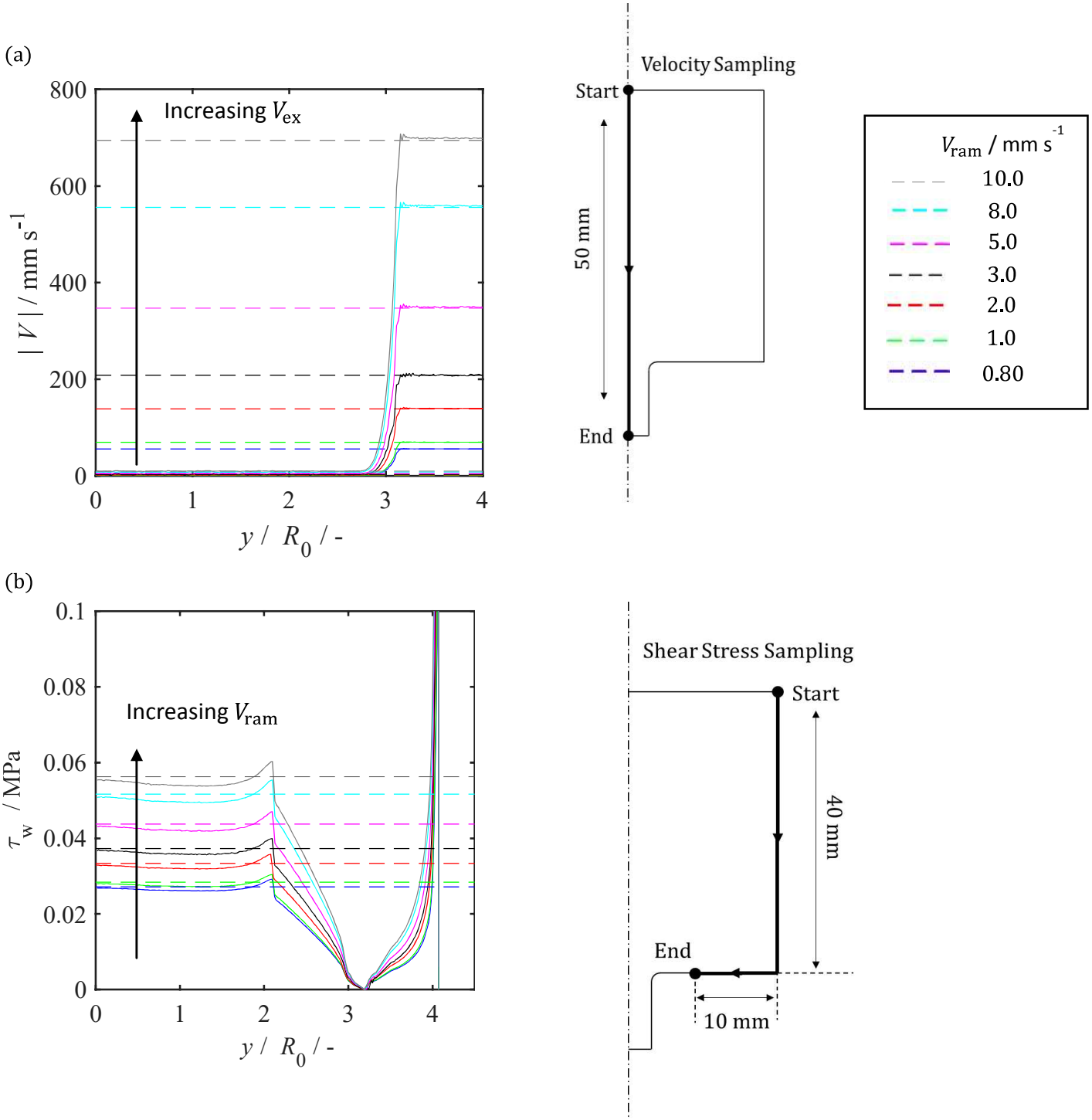

Figure 15. Simulations of square entry simulation with power law friction for V_{ram}values indicated in the legend. (a) Velocity profile along the centreline of the extruding material, (b) Wall shear stress along the barrel wall and die face. Dashed lines in (a) show estimated V_{ex}; those in (b) show frictional shear stress calculated at V_{ram}. Schematic diagrams of the sampling elements are shown alongside each figure. Note that y denotes the distance along the sampling path.

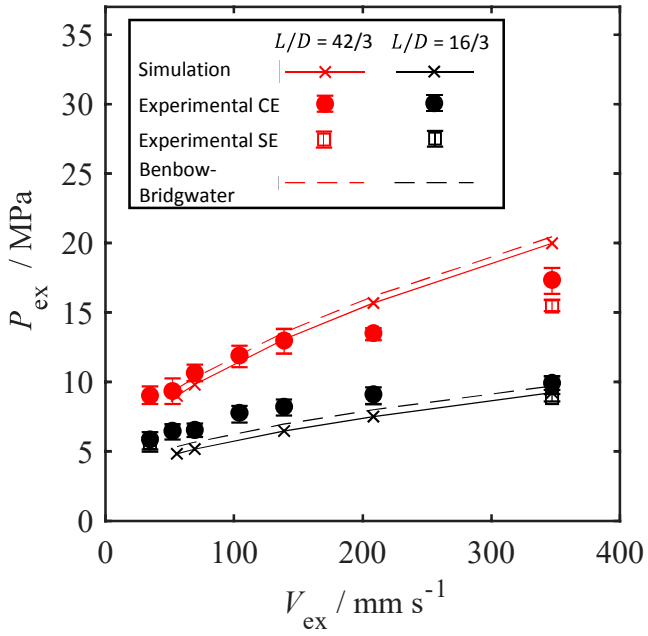

Figure 16. Effect of extrusion velocity on extrusion pressure for conical entry (CE) insert experiments with V_{ram}= 0.8, 1, 2, 3, 5 mm s^{-1} and L/D = 42/3 (red) and 16/3 (black). Symbols - experimental results; solid lines - simulations (with barrel and die land friction corrections), dashed lines – Benbow-Bridgwater, Equation (14), prediction with $\vartheta_{\mathrm{max}} = 45°$. Experimental values for square entry tests are shown as open symbols.

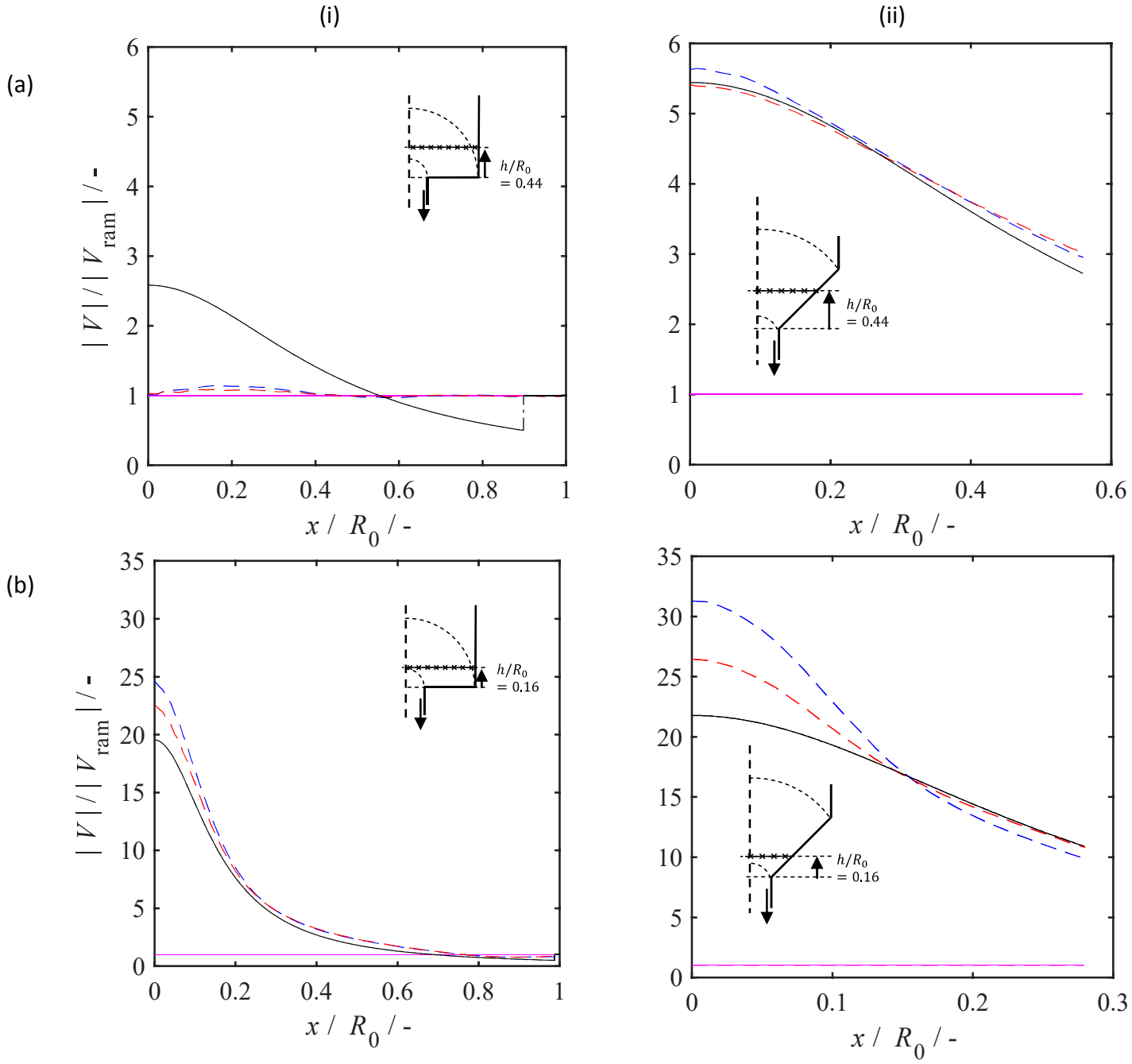

Figure 17. Magnitude of the local flow velocity, sampled across a horizontal plane in the barrel for ((a,i), (b,i)) square-entry and ((a,ii), (b,ii)) conical-entry simulations for the case with $V_{\mathrm{ram}} = 1$ mm s^{-1}. Inserts indicate plane location, $h/R_0 = 0.44$ and 0.16. The velocity magnitude is normalised by the ram velocity, the radial location normalised by the barrel radius (and thus does not extend to 1). Solid black lines show the profiles for the radial flow field used by Basterfield *et al*. (Basterfield, Lawrence and Adams, 2005), with the dot-dash portion representing the velocity discontinuity at the boundary. The horizontal solid purple line indicates the ram velocity. Dashed lines show simulation results: blue – wall friction given by Equation (8); red – smooth wall.